

Nitrogen-Vacancy Centers in Diamond: Nanoscale Sensors for Physics and Biology

Romana Schirhagl, Kevin Chang, Michael Loretz,
and Christian L. Degen

Department of Physics, ETH Zürich, 8093 Zürich, Switzerland; email: degenc@ethz.ch

Annu. Rev. Phys. Chem. 2014. 65:83–105

First published online as a Review in Advance on
November 21, 2013

The *Annual Review of Physical Chemistry* is online at
physchem.annualreviews.org

This article's doi:
10.1146/annurev-physchem-040513-103659

Copyright © 2014 by Annual Reviews.
All rights reserved

Keywords

NV center, fluorescent biomarker, optically detected magnetic resonance (ODMR), nanoscale sensing, quantum sensing

Abstract

Crystal defects in diamond have emerged as unique objects for a variety of applications, both because they are very stable and because they have interesting optical properties. Embedded in nanocrystals, they can serve, for example, as robust single-photon sources or as fluorescent biomarkers of unlimited photostability and low cytotoxicity. The most fascinating aspect, however, is the ability of some crystal defects, most prominently the nitrogen-vacancy (NV) center, to locally detect and measure a number of physical quantities, such as magnetic and electric fields. This metrology capacity is based on the quantum mechanical interactions of the defect's spin state. In this review, we introduce the new and rapidly evolving field of nanoscale sensing based on single NV centers in diamond. We give a concise overview of the basic properties of diamond, from synthesis to electronic and magnetic properties of embedded NV centers. We describe in detail how single NV centers can be harnessed for nanoscale sensing, including the physical quantities that may be detected, expected sensitivities, and the most common measurement protocols. We conclude by highlighting a number of the diverse and exciting applications that may be enabled by these novel sensors, ranging from measurements of ion concentrations and membrane potentials to nanoscale thermometry and single-spin nuclear magnetic resonance.

NV center:
nitrogen-vacancy color
center in diamond

EPR: electron
paramagnetic
resonance

1. INTRODUCTION

Color centers are fluorescent lattice defects that consist of one or several impurity atoms or vacant lattice sites and that are uniquely identified by their optical emission and absorption spectra. Color centers in diamond have been intensively studied for decades, as they are responsible for the typical coloration of diamond gemstones, and several hundred defects have been identified to date (1). Whereas early investigations focused on natural diamond, synthetic material has become increasingly available since the 1950s, and most diamond produced today is consumed by industrial applications that take advantage of the material's superb mechanical hardness, heat conductivity, and optical transparency.

The fields of physics and biology have recently discovered diamond as an ideal material for at least two very different scientific applications. Biologists, on the one hand, have found that diamond nanoparticles show promise as exceptionally robust fluorescent dyes, with many potential applications in biolabeling. Efforts over the past 10 years have led to ~ 4 -nm-sized nanodiamonds with a single fluorescent impurity inside that can be functionalized and internalized by cells without toxic effects (2). Physicists, on the other hand, have made tremendous progress in understanding and controlling the electronic properties of single impurities. One of these impurities, the nitrogen-vacancy (NV) defect, is furthermore magnetic and shows quantum behavior up to room temperature. Spurred by advances in single-molecule fluorescence, the detection of electron paramagnetic resonance (EPR) from a single NV defect was reported in 1997 (3). This initial experiment triggered an intense research effort in the context of quantum information science, and over the past decade, the NV center has become an iconic model system to develop a wide variety of quantum manipulation protocols (4).

This review focuses on a new field of research that has grown out of both the physical and biological groundwork, that of nanoscale sensing or quantum sensing. The idea is to take advantage of the delicate quantum nature of single NV centers to monitor external perturbations, such as magnetic or electric fields, with high sensitivity and spatial resolution. The exciting aspect of diamond impurities is that they are highly stable, even if the host crystal is only a few nanometers in size. This small size provides numerous opportunities to employ them as local probes. In the context of biology, for example, nanodiamonds could simultaneously operate as conventional fluorescent biomarkers and as sensors of the local environment, such as cell potentials. In the fields of materials science and condensed matter physics, NV centers may provide nanoscale-resolution maps of magnetic fields existing near spintronic devices, spin textures, or superconductors.

Before introducing the NV center and its use for nanoscale sensing, we note that several excellent reviews have recently appeared highlighting different aspects of diamond nanoparticles and NV centers. Jelezko & Wrachtrup (4) gave an early overview of NV centers in diamond. More recent and more detailed descriptions of the electronic structure of the NV center were given by Zvyagin & Manson (5) and Doherty et al. (6). Barnard (2) provided an overview of nanodiamonds as fluorescent biomarkers. The properties and applications of nanodiamonds in material science and chemistry were discussed by Mochalin et al. (7) and also by Zvyagin & Manson (5), and the synthesis and use of high-purity bulk material by Balmer et al. (8). Aharonovich et al. (1) gave a systematic overview of color centers in diamond. Finally, Xing & Dai (9) provided a view on nanodiamonds for use in nanomedicine.

This review is organized as follows. In Section 2, we recapitulate the general material properties and surface chemistry of diamond and diamond nanocrystals and their use as fluorescent biomarkers. In Section 3, we give a concise introduction to the electronic, optical, and magnetic properties of the NV color center (NV center). In Section 4, we discuss in detail how NV centers can be harnessed for nanoscale sensing, including the basic experimental protocols, physical

quantities to be measured, and typical sensitivities. The following three sections highlight potential applications in fluorescence microscopy (Section 5), scanning probe microscopy (Section 6), and nanoscale NMR spectroscopy (Section 7). In the last section (Section 8), we discuss the main obstacle toward better diamond probes: surface effects.

NMR: nuclear magnetic resonance
DND: detonation nanodiamond

2. DIAMOND AND NANODIAMONDS

2.1. Synthesis

Diamond is synthesized in the form of nanocrystals, thin films, and bulk crystals. The smallest members of the diamond family are known as diamondoids and are typically extracted from crude oil (10) (see **Figure 1a**). Because diamondoids are too small ($\lesssim 1$ nm) to allow for stable, fluorescent lattice defects in the interior, they are not discussed here.

The next largest type of nanoparticles, so-called detonation nanodiamonds (DNDs), is synthesized by the controlled detonation of TNT-like explosives in a closed vessel (7) (**Figure 1b**). DNDs are core-shell-type particles of 4–5-nm diameter with an sp^3 core surrounded by a few atomic layers of sp^2 carbon. DNDs are quite monodisperse and of small size, which makes them attractive especially for applications in biology, but they are difficult to deaggregate and contain a high proportion of sp^2 -like carbon (7). Recently, DND-like nanodiamonds have also been synthesized using pulsed laser ablation (11), which may offer better control over reaction conditions.

A much purer variety of nanodiamonds can be obtained by grinding large crystals to sub-100-nm-sized particles (**Figure 1c**). These nanodiamonds are size selected by ultracentrifugation and dynamic light scattering (12) and are typically much purer than DNDs. Currently, the smallest commercially available nanodiamond powders have median particle sizes down to ~ 15 nm, and particles down to ~ 5 -nm diameter have been produced by research initiatives (13, 14). The downsides of nanodiamonds produced by mechanical grinding are their irregular, jagged shape and comparably large size.

Large single-crystal diamond plates are synthesized either by high-pressure-high-temperature synthesis or, more recently, by chemical vapor deposition (CVD). Plate dimensions up to 10 mm have been realized (8). Large synthetic crystals easily achieve the highest material quality and very low defect concentrations. For crystals grown by CVD, even isotopically controlled material is available. Bulk single-crystal plates lend themselves as substrates for applications in, for example, microfluidics and can be lithographically shaped into nanostructures or nanoparticles (15).

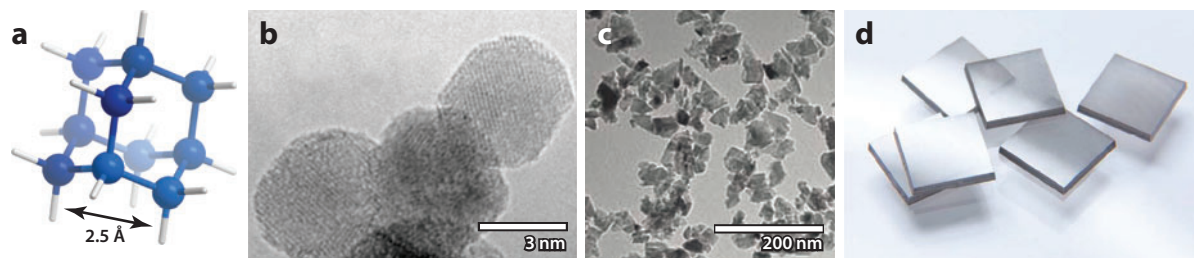


Figure 1

Family of (nano)diamonds. (a) Adamantane, the smallest diamondoid. (b) Transmission electron micrograph of detonation nanodiamonds. Panel b reprinted from <http://adamasnano.com>, accessed June 25, 2013. (c) Scanning electron micrograph of diamond nanoparticles produced by mechanical grinding. Panel c reprinted with permission from Reference 16. (d) Millimeter-sized single-crystal diamond grown by chemical vapor deposition. Panel d reprinted with permission from Reference 17.

Table 1 Comparison of the fluorescent properties of organic dyes, colloidal quantum dots, and single nitrogen-vacancy (NV) centers in nanodiamonds^a

Property	Typical organic dye (20)	Quantum dot (20)	Nanodiamond (NV center)
Size	<1 nm	3–10 nm	>4 nm (13, 19)
Emission spectrum	IR-UV	IR-UV, selected by size	Fixed at approximately 630–800 nm
Emission line width (FWHM)	35–100 nm	30–90 nm	>100 nm
Absorption cross section	Typically $1 \times 10^{-16} \text{ cm}^2$	Typically $3 \times 10^{-15} \text{ cm}^2$	$3 \times 10^{-17} \text{ cm}^2$ (5)
Quantum yield	0.5–1.0	0.1–0.8	0.7–0.8
Lifetime	1–10 ns	10–100 ns	25 ns (6)
Photostability	Low	High	Extremely high ^b
Thermal stability	Low	High	Extremely high ^c
Toxicity	From low to high	Not well known	Low (36)

^aAbbreviations: IR-UV, infrared-ultraviolet; FWHM, full width at half maximum.

^bUsually unlimited (>days), although blinking or bleaching has been reported on a few occasions (97).

^cReported up to above 300°C (102).

2.2. Fluorescent Nanodiamonds

If of high purity and properly cleaned, diamond is colorless and fully transparent. Coloration is introduced by specific lattice impurities and dopants, also known as color centers. Several hundred diamond defects are known, and the investigation of their structure and physical properties continues to be a topic of active research (1).

This review focuses on one particular color center in diamond, known as the NV center. The NV center is formed by a nitrogen atom and adjacent lattice vacancy. The NV center is one of the most common defects in diamond, after simple vacancies and substitutional nitrogen. What sets the NV center apart from other color centers is that it is magnetic (i.e., of nonzero spin) and that the luminescence is coupled to the spin state, such that the luminescence intensity can be modulated by magnetic fields. This magneto-optic property is unique among color centers, and there are only few other examples (18). That said, many diamond color centers lend themselves as fluorescent emitters if the magneto-optic property is not required, including chromium-related centers, the silicon-vacancy center, and hydrogen-related defects (1).

Nanodiamonds can also exhibit fluorescence that is not diamond related. Graphite shells and amorphous carbon on the nanodiamond surface can both create fluorescence and actively quench the fluorescence from color centers in the interior (13). Especially for DNDs, surface fluorescence can be much larger than the color-center fluorescence (19). Many procedures to clean the surface of unwanted sp^2 residues have been introduced based on selective oxidation of sp^2 carbon versus the more stable sp^3 carbon (21). A summary of the fluorescent properties of nanodiamonds as compared to quantum dots and typical organic dyes is given in **Table 1**.

2.3. Generation of Fluorescent Defects

Most diamond contains a certain concentration of natural NV centers. Although the natural NV concentration is sufficient for some applications, most uses require much higher concentrations than those provided naturally. For example, in commercial nanodiamond powders with a median

particle size of ~ 25 nm, less than 1 out of 1,000 nanodiamonds actually hosts an NV center (21). The concentration of NV centers can be much enhanced by high-energy electron or ion irradiation and high-temperature ($\geq 800^\circ\text{C}$) annealing. High-energy irradiation creates a large number of vacancies, and annealing promotes the formation of NV centers through vacancy diffusion. Researchers have reported conversion efficiencies from nitrogen to NV in the 10% range and NV densities of tens of parts per million (14, 22), corresponding to a few NV centers in a 10-nm particle. Alternatively, for bulk crystals, high concentrations of nitrogen can be introduced by ion implantation (23) or by deliberate doping during CVD growth (24). Both ion implantation and doping provide excellent routes to create very shallow, near-surface NV centers, with the shallowest reported depths of less than 5 nm (25, 26).

2.4. Surface Chemistry and Biolabeling

The most common surface termination of diamond is oxygen termination. Chemically, oxygen termination is not well defined and refers to a mixture of $=\text{O}$, $-\text{OH}$, $-\text{COOH}$, or $-\text{C}-\text{O}-\text{C}$ groups on the surface, with slight differences between them (27). Oxygen termination is particularly useful as it renders the surface hydrophilic, results in well-dispersed nanoparticles in aqueous suspension, and is easily established through a range of surface oxidation procedures (21). Moreover, NV centers in oxygen-terminated diamond do show the highest charge stability for shallow defects and small nanodiamonds (28). Other simple surface terminations occasionally explored include hydrogen termination, halogenation by fluorine or chlorine, thermal annealing to create double bonds, and reduction to OH termination (29).

Several protocols have been introduced to modify the diamond surface toward biofunctionalization (27). Carboxy groups can react with alcohols or amine derivatives (30). The reduction of oxygen groups to OH by borane allows for grafting of a variety of silanes (31) or long alkyl chains (32). Halogenated diamond can react with nucleophilic reagents (e.g., lithium organic compounds) in substitution reactions leading to amino or acid terminations (33). In this way, linker molecules, such as *N*-hydroxysuccinamide (34), can be attached. Such molecules provide good leaving groups that are easily replaced and thus readily react with different biomolecules.

Biolabeling can be achieved by two approaches. The easier route is the electrostatic (noncovalent) attachment between the diamond particle and biomolecules (35). Because electrostatic bonding is rather weak and nonspecific, biomolecules often detach under biological conditions. Alternatively, biomolecules such as antibodies (36), biotin/streptavidin (31), aptamers (37), or DNA (37) can be bonded covalently via different linker molecules. **Figure 2** shows examples of fluorescent labeling of cells and other biological systems. Initial experiments have focused on particle uptake and the assessment of cytotoxicity (36). Faklaris et al. (38) studied the uptake mechanism into HeLa cells by applying different surface coatings. In conclusion from their experiments, uptake was attributed to endocytosis. Although the cytotoxicity of nanodiamonds per se was found to be low (34, 36), the sharp etches of the larger and irregular particles produced by mechanical grinding can disrupt delicate cellular structures. A few initial experiments have also demonstrated specific attachment to biomolecules and their use as biolabels in cells. Chao et al. (39) bonded nanodiamonds to lysozyme to target a growth hormone receptor on the surface of lung epithelial cells. Mkandawire et al. (40) achieved targeting of the cytoskeleton by conjugating anti-actin antibodies to nanodiamonds.

3. THE NITROGEN-VACANCY CENTER

3.1. Electronic Structure

The electronic structure of the NV center involves six electrons. Two are provided by the nitrogen atom, and another three are dangling bonds from the three carbon atoms surrounding the vacancy.

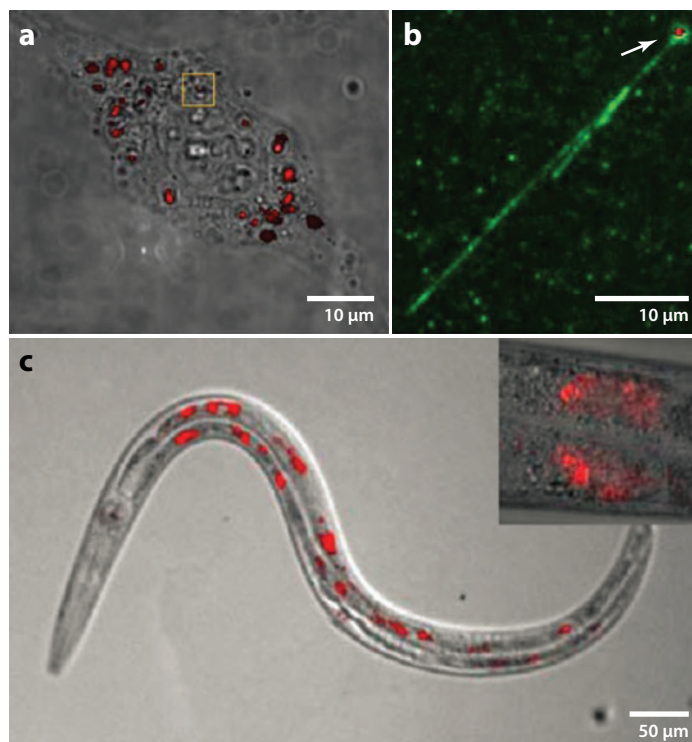


Figure 2

(a) HeLa cell with fluorescent nanodiamonds (red). (b) Single nanodiamond (white arrow) bound to a DNA molecule. Panels a and b reprinted with permission from Reference 36. (c) *Caenorhabditis elegans* fed with dextran-coated fluorescent nanodiamonds (red). (Inset) A 100× magnified image showing nanodiamonds within the intestinal cells. Panel c reprinted with permission from Reference 34.

The sixth electron is captured from the lattice (typically, nitrogen donors), making the overall charge state NV^- . The electron density is mostly located in a plane vertical to the main NV axis, with the highest density on the three carbon atoms and the vacant site (see **Figure 3**) (41, 42). Although two other charge states exist, including the neutral NV^0 and the positively charged NV^+ , neither is magneto-optically active, and virtually all experiments carried out on NV centers refer to the negative NV^- charge state. Conversion of NV^- to neutral NV^0 , however, presents a major challenge toward the generation of high concentrations of very shallow (<10 nm) NV^- centers (see Section 8).

3.2. Optical Properties

A simple energy-level diagram of the NV center, devoid of all nonessential features, is shown in **Figure 4a** (for a detailed description, see 6). The basic photophysics can be explained by three electronic levels, including a ground state $|g\rangle$ of symmetry 3A_2 , an excited state $|e\rangle$ of symmetry 3E , and a metastable singlet state $|s\rangle$ that involves two levels with symmetries 1A_1 and 1E . The ground and excited states are spin triplet ($S = 1$) and are further split into three spin sublevels. The main $|g\rangle \leftrightarrow |e\rangle$ transition has a resonant wavelength of 638 nm (zero phonon line) and can be efficiently excited at most wavelengths below 640 nm. Only a few percent of the photons are emitted into the zero phonon line, and most luminescence appears in vibrational side bands between

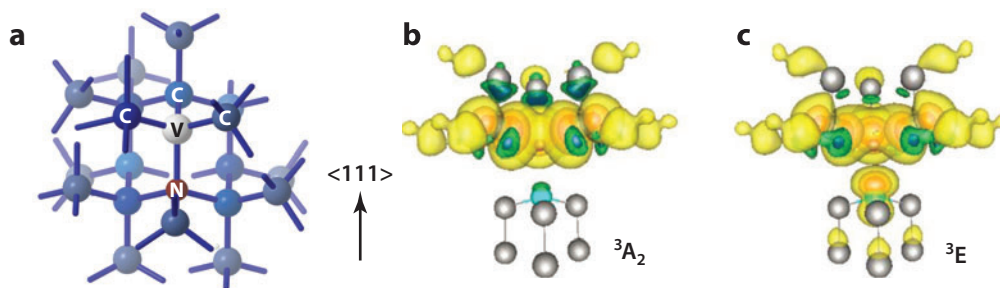


Figure 3

(a) Lattice structure of the nitrogen-vacancy center. (b,c) Three-dimensional electron density of the 3A_2 electronic ground state and the 3E excited state. Panels b and c reprinted with permission from Reference 41.

630 and 800 nm (see **Figure 4b**). The radiative lifetime of the excited state is approximately 13 ns for NV centers in bulk diamond (6, 43) and approximately 25 ns for NV centers in nanodiamonds (6, 44), owing to the different index of refraction. The lifetime of the metastable singlet state is approximately 250 ns (6, 45). The quantum yield, defined as the percentage of excited electrons that decay via the radiative triplet-triplet transition, is approximately 70–80% (6) and is dependent on the spin state.

3.3. Spin Properties

The two triplet states are further split into three spin sublevels. Because of the axial symmetry of the NV center, the two $m_S = \pm 1$ states are degenerate, and the $m_S = 0$ state is energetically lower. The energy difference between spin sublevels is $D = 2.87$ GHz for the ground state and $D = 1.42$ GHz for the excited state, where D is the so-called zero-field splitting (6). The transition rate between $m_S = 0$ and $m_S = \pm 1$ sublevels is given by the spin-lattice relaxation time T_1 and is a few milliseconds at room temperature (46). The degeneracy between $m_S = 0$ and $m_S = \pm 1$ can be lifted by magnetic fields, causing the $m_S = \pm 1$ levels to shift in opposite directions (**Figure 4a**, inset). This magnetic field dependence forms the basis of all magnetic sensing applications. Optical transitions are strongly spin preserving, meaning that the spin state does not change while cycling between $|g\rangle$ and $|e\rangle$ (5).

The metastable singlet state $|s\rangle$ plays a pivotal role in the magneto-optic behavior of the NV center. To begin, $|s\rangle$ is mainly populated from $|e, m_S = \pm 1\rangle$ owing to differing cross-over rates (**Figure 4a**). Thus, an electron in the $|e, m_S = \pm 1\rangle$ state has a significant chance to decay via the long-lived singlet state, whereas an electron in $|e, m_S = 0\rangle$ mostly decays via the fast radiative transition. This leads to an optical contrast between the $m_S = 0$ and $m_S = \pm 1$ states of approximately 30%. The optical contrast is only temporary and disappears for long laser illumination, as decay via the $|s\rangle$ singlet state always repumps the electron to $m_S = 0$. **Figure 4c** plots a histogram of photon emission during a 2- μ s laser pulse that shows the initial peak due to rapid radiative transitions followed by a slow recovery due to singlet decay.

3.4. Optically Detected Magnetic Resonance

Spin-dependent luminescence can be used to perform EPR experiments on a single electron spin, demonstrated in a hallmark experiment by Wrachtrup and coworkers (3) in 1997. The most basic

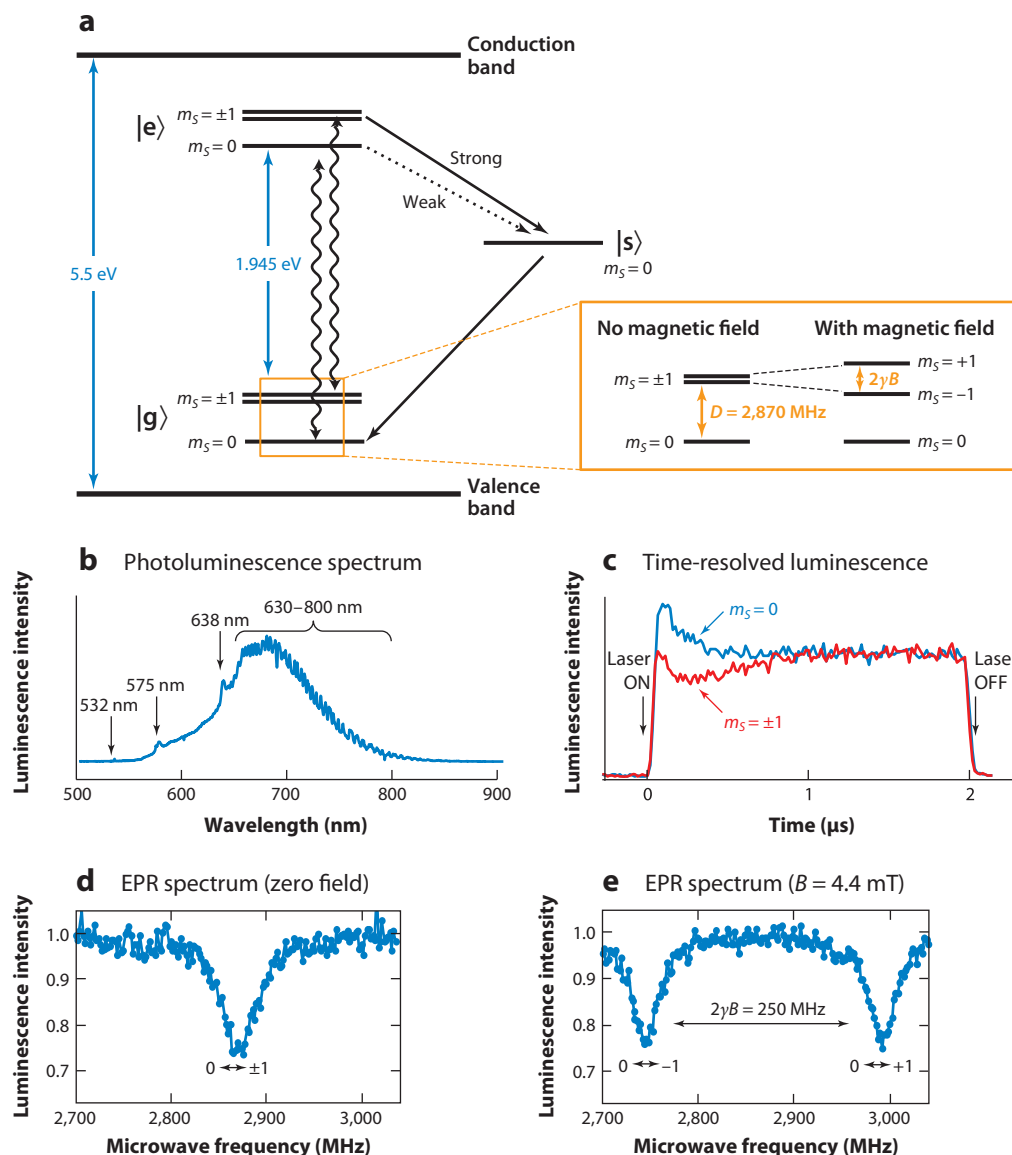


Figure 4

Characteristics of the nitrogen-vacancy (NV^-) center. (a) Energy-level diagram of NV^- . $|g\rangle$ denotes the electronic ground state, $|e\rangle$ the electronic excited state, and $|s\rangle$ the metastable singlet state. Wiggly arrows indicate the radiative transition, and black arrows indicate strong and weak nonradiative decay via the singlet state. (Inset) The three spin sublevels with $m_S = 0$ and $m_S = \pm 1$ at zero and nonzero magnetic field B . D is the zero-field splitting and $2\gamma B$ is the Zeeman splitting, where γ is the electron gyromagnetic ratio. By convention, the lower energy transition is associated with $m_S = -1$. (b) Photoluminescence spectrum of an ensemble of NV centers, showing excitation laser (532 nm), the NV^0 zero phonon line (575 nm), the NV^- zero phonon line (638 nm), and NV^- vibrational side bands (630–800 nm). In typical experiments, nonresonant excitation at 532 nm is used, and luminescence is collected between 630 and 800 nm. (c) Time-resolved luminescence during a 2- μs laser pulse. The curves show histograms of photon counts for an NV center excited out of the (blue) $m_S = 0$ and (red) $m_S = \pm 1$ spin state. (d,e) Electron paramagnetic resonance (EPR) spectrum of a single NV center at zero and nonzero magnetic field, recorded using the optically detected magnetic resonance technique.

experiment is to record the EPR spectrum of the NV center by slowly sweeping an auxiliary microwave field over the EPR resonance. As the microwave frequency is resonant with the EPR transition, excitation from $m_S = 0$ to $m_S = \pm 1$ occurs, resulting in a reduction of fluorescence intensity (see **Figure 4d**). This so-called optically detected magnetic resonance (ODMR) effect is characteristic of NV centers and has only been observed for a handful of other molecules or defects (47). ODMR experiments can be carried out under both continuous illumination and microwave excitation, or in pump-probe experiments. The former are technically simpler and offer higher photon counts, whereas the latter permit the use of sophisticated pulsed magnetic resonance techniques.

ODMR: optically detected magnetic resonance

MRI: magnetic resonance imaging

4. NANOSCALE SENSING

The ODMR effect provides a means to modulate the fluorescence intensity dependent on the (magnetic) interactions of the single electron spin. This feature has formed the basis of several recent proposals aimed at utilizing the NV center to measure magnetic fields and other physical quantities with high sensitivity and nanoscale spatial resolution (48, 49). The magnetic field sensitivity is easily recognized from **Figure 4d,e**: As a magnetic field is applied, two resonances appear in the ODMR spectrum because the degeneracy between the $m_S = \pm 1$ levels is lifted. The frequency separation between the two resonances is given by $2\gamma B_z$, where $\gamma = 2\pi \times 28 \text{ GHz/T}$ is the electron gyromagnetic ratio and B_z is the magnetic field parallel to the NV axis. Thus, measurements of the ODMR frequency immediately yield the absolute value of the magnetic field. This principle of magnetic field sensing is well known from atomic vapor magnetometers (50) and field homogeneity probes in clinical magnetic resonance imaging (MRI) tomographs (51), which achieve <1-pT sensitivities using millimeter-sized probe cells. The particularly exciting aspect of the NV center is that similar measurements can be performed on single spins that are localized within a few angstroms.

Since the inception of NV-based magnetic sensing in 2008 by several groups (including ours) (48, 49, 52), applications of the technique to several other physical quantities have been proposed or demonstrated. Examples include magnetic moments (electron spins, nuclear spins) (25, 53–55), electric fields (56, 57), charge, voltage, current, orientation (37, 58), strain, temperature (59–63), and pressure (64), and yet more physical quantities can be envisioned. In the following, we discuss the basic interactions of the NV center giving rise to these sensing modalities and review the most important experimental protocols to measure these interactions. Sections 5–7 then highlight a number of specific applications.

4.1. Spin Hamiltonian

To understand how different perturbations affect the spin energy levels and cause shifts in the EPR frequencies, one needs to inspect the NV center's spin Hamiltonian (4, 56):

$$\frac{\mathcal{H}}{\hbar} = \underbrace{D \left(S_z^2 - \frac{2}{3} \right)}_{\text{zfs}} + \underbrace{\gamma \mathbf{B} \cdot \mathbf{S}}_{\text{magnetic}} + \underbrace{\epsilon_z E_z \left(S_z^2 - \frac{2}{3} \right) + \epsilon_{xy} \{ E_x (S_x S_y + S_y S_x) + E_y (S_x^2 + S_y^2) \}}_{\text{electric}}. \quad (1)$$

Here, $D = 2.87 \text{ GHz}$ is the zero-field splitting (zfs), \mathbf{B} is a vector magnetic field, $\mathbf{E} = \{E_x, E_y, E_z\}$ is a vector electric field, and ϵ_z and ϵ_{xy} are coupling constants. By convention, the NV center's main axis is along the z axis, or the (111) crystal axis (see **Figure 3**). This Hamiltonian neglects a number of interactions that are not important here, namely hyperfine interactions to the nitrogen and to nearby carbon nuclear spins. At low magnetic fields ($B \ll 100 \text{ mT}$), which are typical for most experiments, the zero-field splitting is the dominant interaction.

Table 2 Coupling coefficients and typical sensitivities

Property	Coupling coefficient		Typical sensitivity ^a	Reference(s)
Magnetic field ^b	γ	28 GHz/T	$0.36 \mu\text{T}/\sqrt{\text{Hz}}$	48, 49, 52, 74
Electric field ^b	ϵ_z	0.17 Hz/(V/m)	$5.8 \text{ kV cm}^{-1}/\sqrt{\text{Hz}}$	56, 57
Electric field ^c	ϵ_{xy}	$3.5 \times 10^{-3} \text{ Hz}/(\text{V/m})$	$280 \text{ kV cm}^{-1}/\sqrt{\text{Hz}}$	56, 57
Strain ^d	$\sim \epsilon_{xy}/d^c$	$\sim 10^{11} \text{ Hz}/(\delta l/l)$	$\sim 10^{-7}/\sqrt{\text{Hz}}$	67
Orientation ^e	γB	100 kHz/°	$0.1^\circ/\sqrt{\text{Hz}}$	37, 48
Temperature	$\partial D/\partial T$	−74 kHz/K	$0.13 \text{ K}/\sqrt{\text{Hz}}$	59, 61–63
Pressure	$\partial D/\partial P$	1.5 kHz/bar	$6.8 \text{ bar}/\sqrt{\text{Hz}}$	64

^aTypical sensitivity for DC detection as shown in **Figure 5b**, assuming a frequency resolution of $10 \text{ kHz}/\sqrt{\text{Hz}}$.

^bLongitudinal ($\theta = 0^\circ$), where θ is the angle between the nitrogen-vacancy axis and the electric field.

^cTransverse ($\theta = 90^\circ$).

^d $d \approx 3 \times 10^{-13} (\text{V/m})^{-1}$ is the local piezoelectric coupling coefficient (67).

^eAt a transverse magnetic field of 1 mT.

We can analyze the Hamiltonian in terms of external perturbations and coupling parameters. Magnetic and electric fields directly act on the spin through the magnetic and electric terms in the Hamiltonian, with a vectorial dependence. Thus, changes in both magnitude and orientation can be measured. Inspection of the coupling parameters (see **Table 2**) shows that the magnetic interaction, caused by the Zeeman effect, is far stronger than the electric interaction, caused indirectly by the Stark effect and spin-orbit coupling (57). Thus, the NV center is very sensitive to magnetic fields but is only moderately sensitive to electric fields when compared to semiconductor quantum dots, for example. [We note that much better electric field sensitivities could be achieved by high-resolution optical spectroscopies at cryogenic temperatures (65) and that all-optical magnetic field measurements based on nickel-related centers have been demonstrated (66).]

Energy levels can also be perturbed by a number of other physical quantities via the zero-field-splitting parameter D . The zero-field splitting is a consequence of the confinement of the electronic wave function and sensitively responds to crystal compression and expansion, as well as to the vibrational motion of surrounding atoms. Examples of quantities affecting D are pressure, strain, and temperature. Several coupling constants have been theoretically or experimentally determined and are collected in **Table 2**.

4.2. Sensing Protocols

A diverse set of experimental protocols has been conceived to precisely measure EPR frequency shifts caused by these external perturbations. The three most common approaches are the direct detection of the EPR spectrum using continuous-wave spectroscopy, the measurement of the time evolution in (pulsed) pump-probe experiments, and measurements of spin relaxation times.

4.2.1. Continuous-wave experiments. The most direct, yet rather insensitive, frequency measurement is the recording of the EPR spectrum and fitting for the center position of the resonance line. **Figure 5a** shows example data in which fitting of the ($m_S = 0$, $m_S = -1$) EPR transition was used to determine the magnitude of two slightly different external magnetic fields. In cases in which there are small frequency shifts and the EPR resonance frequency is well known, one can maximize the sensitivity by tuning the microwave frequency to the point of highest slope

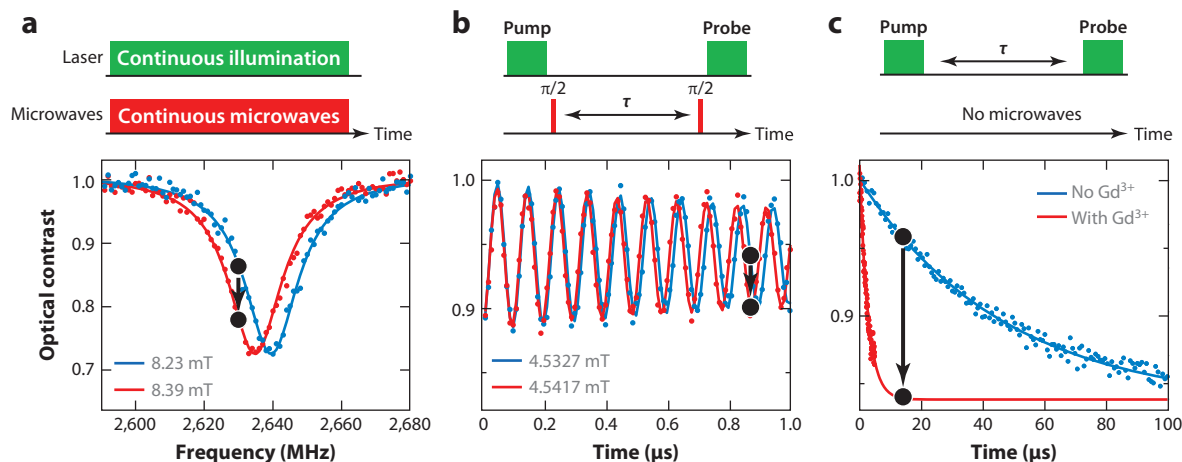


Figure 5

Sensing techniques and protocols, showing (*top*) pulse-timing diagrams and (*bottom*) example measurements. (*a*) Continuous-wave detection of the spectral line shift. The frequency difference between curves is 4.7 MHz, corresponding to a magnetic field difference of 0.16 mT. (*b*) Pulsed detection of the spin precession (Ramsey fringes) in a pump-probe experiment. The frequency difference between curves is 0.25 MHz, corresponding to a magnetic field difference of 9.0 μ T. Oscillations are shown relative to a 2,753-MHz carrier frequency. (*c*) Relaxometry measurement, showing T_1 relaxation of a nitrogen-vacancy center in a 25-nm nanodiamond in the presence and absence of paramagnetic GdCl₃ salt. The black dots mark changes in intensity caused by tuning the microwave frequency to the point of highest slope. The black arrows denote the increase and decrease in fluorescence intensity as the resonance shifts up and down in frequency, respectively.

and recording changes in intensity. As the resonance shifts up or down in frequency, the fluorescence intensity is raised or lowered, respectively. The smallest detectable frequency shift (at unit signal-to-noise ratio) is approximately given by

$$\Delta\omega \approx \frac{a}{2\eta\sqrt{I_0T}}, \quad (2)$$

where a is the line width (0.5 times the full width at half maximum) of the EPR transition, $\eta \approx 30\%$ is the optical contrast between $m_S = 0$ and $m_S = \pm 1$, I_0 is the photon count rate, and T is the integration time. For the example in **Figure 5a**, $a \approx 9.5$ MHz, $\eta \approx 29\%$, and $I_0 \approx 5 \times 10^4$ s⁻¹, yielding $\Delta\omega \approx 2\pi \times 73$ kHz for a 1-s integration time. The sensitivity can be drastically improved by collecting photons from many NV centers simultaneously (ensemble magnetometry) at the expense of losing the exquisite nanoscale resolution provided by single defects.

Frequency detection has been extended by several tricks, including real-time tracking (68), multifrequency excitation (69), and the detection of multiple NV centers with different crystallographic orientations for vector field measurements (70, 71). Moreover, by using large ensembles of NV centers in bigger crystals, investigators have achieved detection rates up to megahertz and sensitivities below kHz/ $\sqrt{\text{Hz}}$ (72).

4.2.2. Pulsed experiments. More sensitive approaches rely on pulsed experiments in a pump-probe scheme with the laser turned off during the sensing period. The advantage of pulsed experiments is that no optical repumping occurs during the sensing period, and very long coherent evolution times τ can be achieved (up to milliseconds) (48, 49). Moreover, pulsed experiments can take advantage of the many refined microwave sequences that have been developed over the decades in the field of magnetic resonance (73).

T_2^* : spin dephasing time

T_2 : spin echo decay time; decoherence time

T_1 : spin-lattice relaxation time

Figure 5b shows an example of pulsed magnetometry in a Ramsey (or free-induction-decay) experiment. The spin is pumped into the $m_z = 0$ state using a laser pulse and free, coherent precession initiated by a resonant $\pi/2$ microwave pulse. After evolution time τ , the precession is halted by a second $\pi/2$ microwave pulse, and the spin state is read out by a second laser pulse. This sequence is repeated typically millions of times until sufficient photons have been collected. Plotting the signal intensity for a series of τ reproduces oscillations (Ramsey fringes) with a frequency equal to the EPR transition frequency yielding the absolute value of the magnetic field.

The sensitivity of pulsed detection is directly proportional to the coherent evolution time τ , also referred to as the sensing period. τ takes the role of the inverse line width in Equation 2. The maximum possible τ is set by the spin coherence time, which for the Ramsey sequence is the spin dephasing time T_2^* . T_2^* typically ranges up to a few microseconds, unless isotopically pure diamond is used. As **Figure 5b** clearly illustrates, much enhanced sensitivities are possible with pulsed detection compared to the continuous-wave approach shown in **Figure 5a**.

The basic Ramsey sequence shown in **Figure 5b** is a DC measurement technique that is sensitive to static magnetic fields. Recent efforts have shown that sensitivities can be enhanced by several orders of magnitude by moving to AC detection with signal frequencies in the kilohertz to megahertz range. AC field detection can be achieved using spin echoes. (Another technique is relaxometry, which is introduced in the next section.) For this purpose, the free evolution period is intercepted by a π microwave pulse, leading to a refocusing of static interactions in the Hamiltonian. This corresponds to a rejection of low-frequency noise. Because the spin echo decay is governed by T_2 (and not T_2^*), which can extend up to several hundreds of microseconds in pure crystals, spin echo detections are very sensitive, with demonstrated magnetic field sensitivities of a few nanoteslas (53, 74).

The simple spin echo sequence can be extended to multiple spin echoes that have a narrowband filter profile and even longer coherence times (up to a few milliseconds). In fact, it has been shown that multiple spin echoes act like a narrowband lock-in amplifier whose detection frequency can be chosen by adjusting the interpulse spacing (75). Multiecho protocols have proven instrumental in detecting the megahertz signals from nuclear spins in nanoscale NMR applications (25, 54, 55).

4.2.3. Relaxometry. Even faster megahertz to gigahertz frequency signals can be probed using the techniques of magnetic resonance relaxometry. Magnetic resonance relaxometry makes use of the fact that spin relaxation times (most importantly T_1) directly reflect the amount of magnetic noise occurring at the spin transition frequency. **Figure 5c** illustrates the principle of relaxometry by exposing an NV center embedded in a nanocrystal to paramagnetic Gd^{3+} ions. Measurement of the T_1 relaxation time (using the pump-probe protocol shown in the figure) reveals much faster decay in the presence of Gd^{3+} ions. The fast relaxation is caused by the gigahertz fluctuations of the Gd spin ($S = 7/2$), which cause strong magnetic noise at the NV center EPR frequency (2.9 GHz). That T_1 times can be measured without the need for microwave excitation (see **Figure 5c**) (76) makes them particularly simple and useful.

Relaxometry is not restricted to T_1 measurements. Measurements of the spin-lock decay time $T_{1\rho}$, for example, allow for detection of magnetic signals up to 100 MHz with excellent spectral resolution (<10 kHz) and sensitivity (<100 nT) (77). Moreover, many of the pulse protocols discussed above (such as spin echoes) can be analyzed for their relaxation time.

5. EMERGING APPLICATIONS: OVERVIEW

The prospect of a generic, nanoscale fluorescent probe that is moreover stable and biocompatible has stimulated an extraordinary variety of proposals for applications. A few are highlighted in the

next three sections, starting with those utilizing standard optical microscopy (this section) and continuing with scanning-probe-based techniques (Section 6) and nanoscale NMR (Section 7). **Figure 6** sketches these potential applications and provides a few highlights of the growing experimental work.

5.1. Monitoring Ion Concentrations

Spin relaxometry may enable concentration measurements of paramagnetic ions and molecules in solution. Several proof-of-principle experiments have already demonstrated the effectiveness of common relaxation agents, such as Gd^{3+} ions (76, 78), Mn^{2+} ions (76, 79), and ferritin molecules (80). For example, Steinert et al. (76) demonstrated concentration measurements of Gd^{3+} ions in the millimolar-to-molar range, with a threshold concentration below 1 mM (see **Figure 6b**). They also showed a slight increase in spin relaxation for bare water compared to air. Although only magnetic ions or molecules can be detected by relaxometry, the method has some intriguing prospects, such as the monitoring of paramagnetic oxygen (O_2) or the generation of image contrast by targeted labeling.

5.2. Sensor Arrays for Wide-Field Microscopy

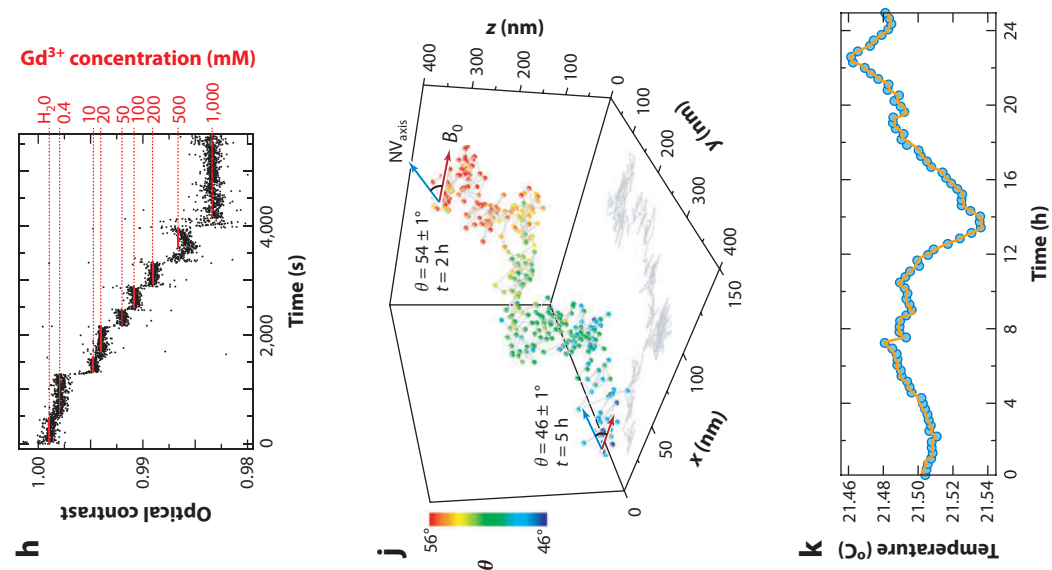
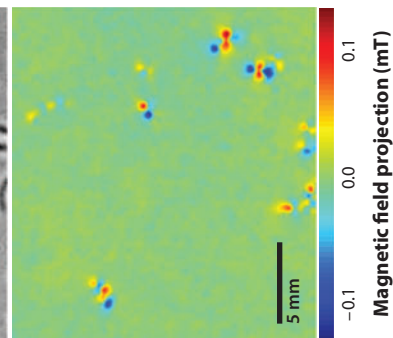
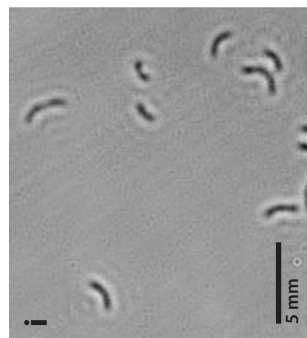
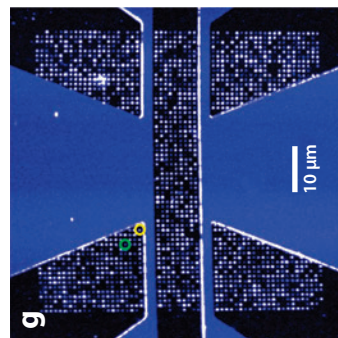
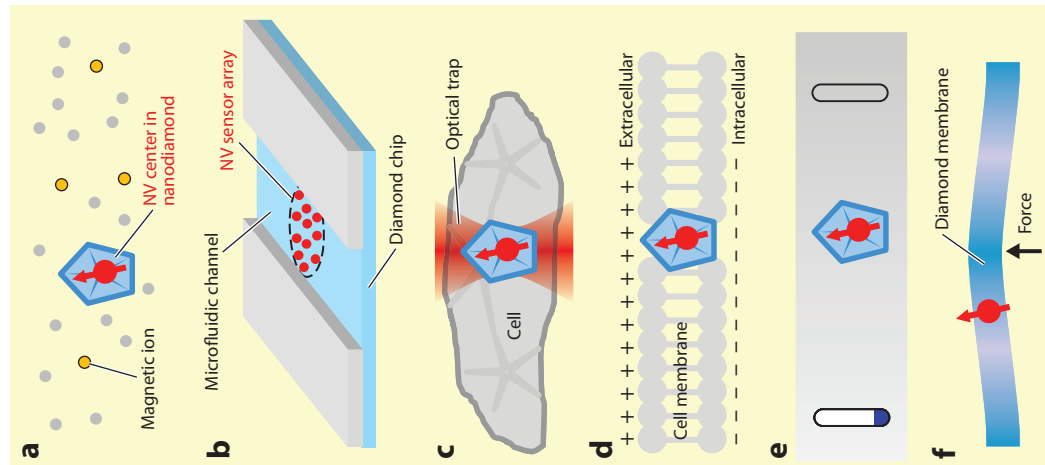
Large-area diamond plates may find applications as sensor arrays in microfluidics and wide-field microscopy. Sensor arrays are millimeter-sized diamond surfaces with a dense layer of shallow ($\lesssim 10$ -nm) NV centers (**Figure 6g**) (81) created by ion implantation (26) or thin-film growth (25). One can then use conventional wide-field microscopy with a CCD (charge-coupled device) detector to simultaneously record a fluorescence image of the entire array. Sensor arrays have been applied for the imaging of magnetosomes in immobilized magnetotactic bacteria (**Figure 6i**) (82), for example, and have been combined with a microfluidic device to monitor ion concentrations (76).

5.3. Optical Trapping

Two experiments demonstrated that nanodiamonds can be optically trapped (83, 84) and that concurrent ODMR measurements are possible. These initial works provide exciting perspectives for nanoscale sensing within living systems. Nanodiamonds could be maneuvered with nanometer precision through the cellular environment so as to perform measurements at desired locations. Interestingly, the experiments showed that trapped nanodiamonds, owing to their nonspherical shape, do not rotate and that the orientation can be controlled at will by the adjustment of light polarization (84). Optical trapping can thus provide full real-time control of both three-dimensional location and orientation. McGuinness et al. (37) further demonstrated that the absolute orientation of nanodiamonds can be tracked independently using the vector dependence of the NV center on magnetic field, achieving a precision of $<1^\circ/\sqrt{\text{Hz}}$ (see **Figure 6j**).

5.4. Measurement of Membrane Potentials

A proposal from our group includes the in situ measurement of membrane potentials based on electric field detection (85). As sketched in **Figure 6**, single nanodiamonds may be embedded in the cell membrane in which they experience a strong potential drop between the intra- and extracellular space. Given typical membrane potentials of 40–80 mV and a membrane thickness of 5–10 nm, the expected electric field is of order 10^7 V/m, and the corresponding ODMR frequency shifts a few megahertz. This strong response should permit monitoring of the millisecond excitation



of neurons in real time, for example. The integration of nanodiamonds into cell membranes has recently been accomplished for an artificial lipid bilayer in another context (86).

5.5. Nanoscale Thermometry

NV centers provide fascinating prospects for nanoscale thermometry, based on the temperature dependence of the zero-field splitting (59). Precise local temperature measurements in living systems could provide a powerful new method in biological research and may be useful tools for many areas of nanoscience and technology (62). Several proof-of-principle experiments have recently defined the limits of the approach with sensitivities better than $10 \text{ mK}/\sqrt{\text{Hz}}$ (see **Figure 6k**) (61, 63) at temperatures from near-absolute zero to more than 200°C (60, 61). Experiments on nanodiamonds ingested in living cells have further underscored the biocompatibility of NV-based thermometry (62). Moreover, thermometry has been combined with local heating to measure temperature gradients at the micrometer scale (62, 63). Apart from spin measurements, the optical contrast (61) and the luminescence lifetime (87) have also been invoked for nanoscale thermometry.

5.6. Strain and Pressure Sensing

NV centers in bulk diamond structures may act as local strain and pressure gauges. Strain sensing could be particularly useful for motion transduction in diamond micro- and nanoelectromechanical systems, with further applications in quantum science and technology. Pressure sensing may offer a convenient way to control conditions in extreme environments, such as in diamond anvil cells that reach pressures up to tens or hundreds of gigapascals (64).

6. EMERGING APPLICATIONS: SCANNING MAGNETOMETRY

Scanning probe microscopy offers an exciting perspective to push the spatial resolution of diamond sensors toward the atomic scale. In fact, most early proposals and demonstrations of NV-center-based sensing emphasized the use of scanning probes (48, 52, 88). The basic idea is to embed an NV center at the apex of a very sharp tip ($<10\text{-nm}$ tip radius) and to scan this tip over the sample of interest (see **Figure 7**). Because the spatial resolution is defined by the distance between the tip and the sample, very high resolution images can be recorded. For scanning NV sensors, the minimum tip-sample distance is limited by how close stable NV centers can be formed to a diamond surface, which is currently approximately 2 nm (see Section 8). This distance has not yet been achieved owing to difficulties involving tip fabrication. There is little doubt, however, that resolutions well below 5 nm will be demonstrated in the near future even if a tip standoff is taken into account.

Figure 6

(a–f) Sketches of promising applications of nitrogen-vacancy (NV) centers for nanoscale sensing and (g–k) first examples from the literature. (a) Monitoring of ion concentration by relaxometry measurements of nanodiamonds in solution. (b) Microfluidic channel integrating an NV sensor array. (c) Optical trapping and maneuvering of nanodiamonds through living cells. (d) Sensing of cell potentials by membrane-embedded nanodiamonds. (e) Nanoscale thermometry. (f) Strain sensing in mechanical diamond membranes. (g) Diamond sensor array created by ion implantation of bulk diamond crystal. Each pixel contains from a single up to a few NV centers. Panel g reprinted with permission from Reference 81. (h) Concentration measurements of Gd^{3+} ions based on relaxometry. Panel h reprinted with permission from Reference 76. (i) Optical wide-field (upper) and magnetic (lower) images of magnetotactic bacteria. Panel i reprinted with permission from Reference 82. (j) Orientation and position tracking of a single nanodiamond over several hours. Panel j reprinted with permission from Reference 37. (k) Monitoring of laboratory temperature over 24 h using a bulk diamond sensor. Panel k reprinted with permission from Reference 63.

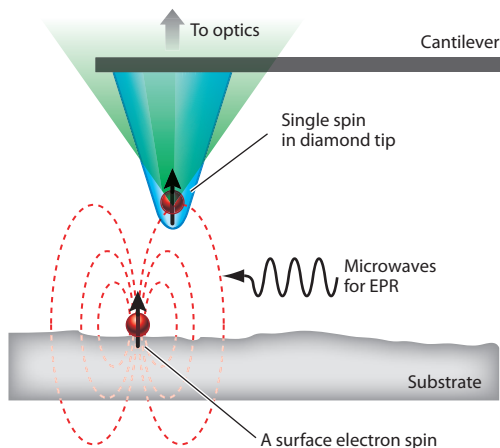


Figure 7

Basic principle of scanning magnetometry. A sharp tip with a nitrogen vacancy center at the apex is used to map out the three-dimensional magnetic field vector above a magnetic nanostructure, such as an isolated electronic spin. Figure reprinted with permission from Reference 48.

The critical element in the scanning magnetometer is the nanoscale tip that incorporates the single NV center. Two techniques for tip fabrications have been explored: pickup of nanodiamonds using commercial atomic force microscopy cantilevers (21, 52, 89) and etching of monolithic tip structures from bulk single crystals (90). The best tip-sample separations reported are approximately 10 nm (53, 90). Although both tip fabrication methods have been successfully used in imaging experiments, tip integration remains a tedious manual process that provides a major obstacle toward routine use of the technique.

Several exciting experiments have recently been reported using prototype scanning magnetometers. Initial demonstrations have mostly focused on magnetic nanostructures. **Figure 8** shows some examples, including the imaging of a magnetic vortex in a thin ferromagnetic film (91), the

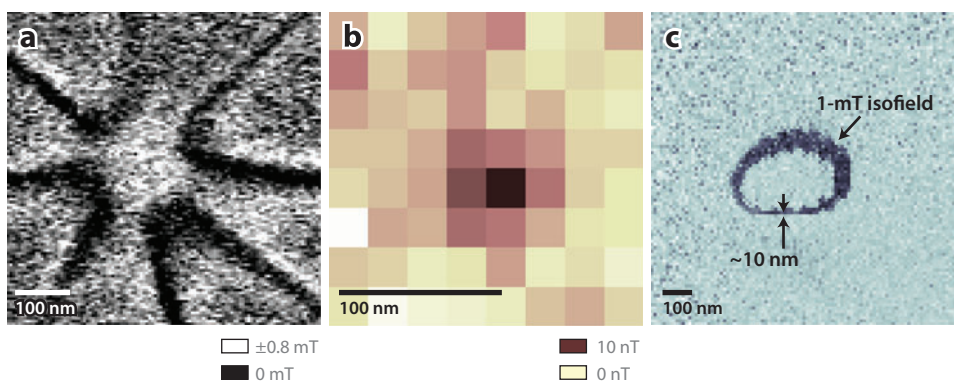


Figure 8

Examples of scanning magnetometry. (a) Magnetic image of a vortex core in a thin ferromagnetic film. Panel *a* reprinted with permission from Reference 91. (b) Magnetic image of the electron spin of a second, immobile NV center from 50 nm away. Panel *b* reprinted with permission from Reference 91. (c) Isofield surface of a magnetic nanotip showing a spatial resolution of <10 nm.

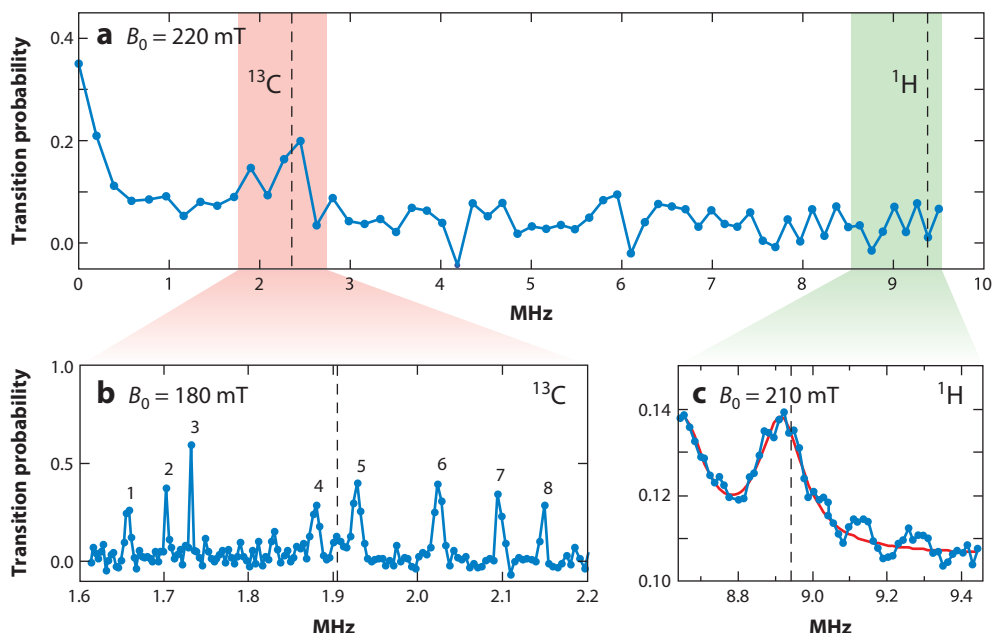


Figure 9

Example of nanoscale nuclear magnetic resonance (NMR) detected by a single nitrogen-vacancy center. (a) Magnetic noise spectrum between 0 and 10 MHz using the spin-locking protocol (77). (b) High-resolution NMR spectrum of single ^{13}C nuclear spins (numbered) located in the diamond crystal. (c) High-resolution NMR spectrum of an ensemble of $\sim 6,000$ ^1H nuclear spins located in organic material deposited on top of the diamond crystal. All spectra were taken at approximately 200 mT. Vertical lines indicate the bare NMR frequency of the respective nuclear spin species. The vertical scale is the transition probability between $|0\rangle$ and $|-1\rangle$ states and is proportional to the power spectral density in units of T^2/Hz . Panel c reprinted with permission from Reference 25.

detection of a single electron spin at a distance of approximately 50 nm (53), and the imaging of a nanoscale magnetic tip with a lateral resolution exceeding 10 nm (85). These initial demonstrations set the stage for applications to a number of interesting nanostructures, ranging from disk drive heads and media to magnetic islands, spin textures, and spintronic devices.

7. EMERGING APPLICATIONS: NANOSCALE NUCLEAR MAGNETIC RESONANCE

One of the most visionary applications of NV-based magnetometry involves the detection and three-dimensional mapping of nuclear spins in nanoscale samples, ultimately with atomic resolution. Such a nanoscale NMR capability is expected to have a profound impact on the structure determination of proteins and other complex biological molecules, and it would be an extremely useful technique for the chemical analysis of surfaces and associated dynamics.

Although no nanoscale imaging experiments of nuclear spins have been reported to date, impressive progress has been made toward the detection of nanoscale NMR signals from few nuclear spins. Initial experiments have focused on ^{13}C nuclear spins naturally embedded (at 1%) in the diamond lattice, resolving up to eight individual nuclei (see **Figure 9b**). The common approach is to place the sample in a relatively high magnetic field (up to a few hundred milliteslas) and to detect the megahertz Larmor precession of the nuclear spins by spin echo techniques (75)

or by spin-lock relaxometry (77) (see Section 4.2). In 2013, nanoscale NMR experiments were extended to nuclear spins exterior to the diamond host crystal, detecting between 10^3 and 10^6 proton nuclei in an organic sample on top of a diamond chip with very shallow NV centers (25, 54, 55) (see **Figure 9c**). The corresponding detection volumes were between $(4\text{ nm})^3$ and $(20\text{ nm})^3$. Even more recently, the detection of as few as approximately 10^{29}Si nuclei in SiO_2 was reported using NV centers as shallow as $\sim 2\text{ nm}$ (92).

Although NMR detection appears poised to reach single spin sensitivity in the near future, achieving three-dimensional imaging resolution will be considerably more challenging. Similar to MRI, magnetic gradients could be introduced to provide imaging resolution (48). Considering that the distance between ^1H spins in organic compounds is only a few angstroms, however, very high gradients in the range of 10^7 – 10^8 T/m will be needed. These gradients are challenging to achieve even for optimized magnetic nanotips (93). Moreover, as the NMR signal from single nuclear spins reduces with the third power of distance, it is questionable whether single spin sensitivity can be reached more than a few nanometers away from a sample. This limits the depth resolution and thus the three-dimensional imaging capability of larger and more complex molecules.

8. SURFACE EFFECTS

Stable NV centers have been observed at a minimum depth of approximately 2 nm from diamond surfaces (92, 94) and in nanocrystals as small as 4 nm (13). At these shallow depths, surface properties can profoundly impact (and deteriorate) the electronic stability and the spin lifetime of the defect. In this section, we briefly review the present understanding of surface effects with shallow NV centers that are crucial toward more sensitive, less invasive, and higher-resolution probes and biomarkers.

Despite the expanse of the electronic wave function of the NV center being less than $(1\text{ nm})^3$ (or $3 \times 3 \times 3$ unit cells) (41, 95), no NV centers have been reported for such small crystals. The main issue with shallow NV centers is the conversion to neutral NV^0 . The mechanism behind charge state conversion is not entirely clear but appears to involve either stable charge traps on the surface or surface band bending (28, 96). Charge transfer to surface traps can be promoted by optical illumination (bleaching) (97). For very shallow NV centers, loss of charge may also occur via quantum mechanical tunneling. In the case of band bending, the location of the Fermi level with respect to the NV^- excited state determines the charge stability of the defect.

Given this picture, several routes have been explored to improve the charge stability of shallow NV centers. Surface termination by oxygen or fluorine, for example, was found to favor NV^- , whereas termination by hydrogen (and, to a minor extent, chlorine) was found to favor NV^0 because of surface band bending (28, 96, 98). Surface band engineering by heavy nitrogen doping of the top 5 nm stabilized NV centers, even for hydrogen-terminated surfaces (25), but did not confirm any NV centers shallower than 2 nm. Moreover, blinking or bleaching was observed both for dispersed (oxygen-terminated) nanodiamonds (97) and for fluorine-terminated surfaces (25), giving no clear clue of the best surface chemistry.

In addition to reduced electronic stability, NV centers near surfaces also experience enhanced magnetic noise that manifests itself in reduced spin relaxation times compared to bulk diamond. This directly compromises detection sensitivity (26). Reduction in spin relaxation times has been observed for nanodiamonds smaller than $\sim 50\text{ nm}$ (99) and for thin-film defects less than $\sim 10\text{ nm}$ from the surface (26). The cause of surface-related magnetic noise is not fully understood and is believed to originate from surface magnetic impurities, such as dangling bonds (100). Reported densities of surface states vary between $0.01\mu_B/\text{nm}^2$ for high-purity crystals with controlled surface chemistry (94) and $10\mu_B/\text{nm}^2$ for nanodiamonds (13). The characteristic correlation time

of surface fluctuations has been measured as 0.28 ± 0.05 ns for bulk crystals (94). Moreover, a different type of surface magnetic impurity has recently been resolved by scanning magnetometry that fluctuates much slower (101). The elimination of surface magnetic impurities will be critical for achieving adequate sensitivity with many proposed applications, in particular for scanning probe measurements and experiments relying on <10-nm nanodiamond sensors.

SUMMARY POINTS

1. Diamond color centers are fluorescent impurities in diamond.
2. The NV center is a color center consisting of a substitutional nitrogen and a lattice vacancy. The luminescence of the NV center is extremely robust, with no bleaching or blinking under normal conditions.
3. NV centers can be embedded in nanocrystals down to 4–5 nm in size. Diamond nanocrystals are chemically very robust, nontoxic, and easily functionalized for biological targeting.
4. The unique features of the NV center are its magnetic (spin triplet) ground state and the dependence of its fluorescence intensity on the spin orientation. This feature is utilized to add (magnetic) sensing capabilities.
5. EPR spectra of single NV centers can be detected by measuring the fluorescence intensity in response to microwave irradiation (ODMR technique).
6. Sensing is performed by monitoring shifts of the EPR spectra due to external perturbations. Perturbations can be generated by many means, including magnetic and electric fields, temperature, spatial orientation, strain, pressure, and other physical parameters.
7. NV centers can be embedded in nanocrystals, sensor arrays, and scanning probe heads, giving rise to an extraordinary variety of possible applications.

DISCLOSURE STATEMENT

The authors are not aware of any affiliations, memberships, funding, or financial holdings that might be perceived as affecting the objectivity of this review.

ACKNOWLEDGMENTS

This work was supported by the Swiss National Science Foundation through project grant 200021_137520/1 and through the NCCR QSIT and by ETH Zürich. R.S. acknowledges a Marie Curie fellowship, and C.L.D. acknowledges the DARPA QuASAR program and the EU DIADEMS program. We thank T. Rosskopf and A. Dussaux for stimulating discussions and F. Jelezko for carefully reading the manuscript.

LITERATURE CITED

1. Aharonovich I, Castelletto S, Simpson DA, Su CH, Greentree AD, Prawer S. 2011. Diamond-based single-photon emitters. *Rep. Prog. Phys.* 74:076501
2. Barnard AS. 2009. Diamond standard in diagnostics: Nanodiamond biolabels make their mark. *Analyst* 134:1751–64

3. Demonstrates the first experiment showing ODMR detection on a single NV center.

13. Presents comprehensive fluorescence and spin measurements on <10-nm-sized nanodiamonds.

3. Gruber A, Dräbenstedt A, Tietz C, Fleury L, Wrachtrup J, von Borczyskowski C. 1997. Scanning confocal optical microscopy and magnetic resonance on single defect centers. *Science* 276:2012–14
4. Jelezko F, Wrachtrup J. 2006. Single defect centres in diamond: a review. *Phys. Stat. Solidus A* 203:3207–25
5. Zvyagin AV, Manson NB. 2012. Optical and spin properties of nitrogen-vacancy color centers in diamond crystals, nanodiamonds, and proximity to surfaces. In *Ultrananocrystalline Diamond*, ed. OA Shenderova, DM Gruen, pp. 327–54. Amsterdam: Elsevier. 2nd ed.
6. Doherty MW, Manson NB, Delaney P, Jelezko F, Wrachtrup J, Hollenberg LC. 2013. The nitrogen-vacancy colour centre in diamond. *Phys. Rep.* 528:1–45
7. Mochalin VN, Shenderova O, Ho D, Gogotsi Y. 2012. The properties and applications of nanodiamonds. *Nat. Nanotechnol.* 7:11–23
8. Balmer RS, Brandon JR, Clewes SL, Dhillon HK, Dodson JM, et al. 2009. Chemical vapour deposition synthetic diamond: materials technology and applications. *J. Phys. Condens. Matter* 21:364221
9. Xing Y, Dai LM. 2009. Nanodiamonds for nanomedicine. *Nanomedicine* 4:207–18
10. Dahl JE, Liu SG, Carlson RMK. 2003. Isolation and structure of higher diamondoids, nanometer-sized diamond molecules. *Science* 299:96–99
11. Amans D, Chénus AC, Ledoux G, Dujardin C, Reynaud C, et al. 2009. Nanodiamond synthesis by pulsed laser ablation in liquids. *Diam. Relat. Mater.* 18:177–80
12. Morita Y, Takimoto T, Yamanaka H, Kumekawa K, Morino S, et al. 2008. A facile and scalable process for size-controllable separation of nanodiamond particles as small as 4 nm. *Small* 4:2154–57
13. Tisler J, Balasubramanian G, Naydenov B, Kolesov R, Grotz B, et al. 2009. Fluorescence and spin properties of defects in single digit nanodiamonds. *ACS Nano* 3:1959–65
14. Boudou JP, Curmi PA, Jelezko F, Wrachtrup J, Aubert P, et al. 2009. High yield fabrication of fluorescent nanodiamonds. *Nanotechnology* 20:235602
15. Hausmann BJ, Khan M, Zhang Y, Babinec TM, Martinick K, et al. 2010. Fabrication of diamond nanowires for quantum information processing applications. *Diam. Relat. Mater.* 19:621–29
16. Havlik J, Petrakova V, Rehor I, Petrak V, Gulka M, et al. 2013. Boosting nanodiamond fluorescence: towards development of brighter probes. *Nanoscale* 5:3208–11
17. Wort CJ, Balmer RS. 2008. Diamond as an electronic material. *Mater. Today* 11:22–28
18. Lee S, Widmann M, Rendler T, Doherty MW, Babinec TM, et al. 2013. Readout and control of a single nuclear spin with a metastable electron spin ancilla. *Nat. Nanotechnol.* 8:487–92
19. Smith BR, Inglis DW, Sandnes B, Rabeau JR, Zvyagin AV, et al. 2009. Five-nanometer diamond with luminescent nitrogen-vacancy defect centers. *Small* 5:1649–53
20. Resch-Genger U, Grabolle M, Cavaliere-Jaricot S, Nitschke R, Nann T. 2008. Quantum dots versus organic dyes as fluorescent labels. *Nat. Methods* 5:763–75
21. Schirhagl R, Chang KK, Loretz M, Degen CL. 2013. A practical guide for preparing fluorescent nanodiamonds. Submitted manuscript
22. Hui YY, Cheng CL, Chang HC. 2010. Nanodiamonds for optical bioimaging. *J. Phys. D* 43:374021
23. Pezzagna S, Naydenov B, Jelezko F, Wrachtrup J, Meijer J. 2010. Creation efficiency of nitrogen-vacancy centres in diamond. *New J. Phys.* 12:065017
24. Ohno K, Heremans FJ, Bassett LC, Myers BA, Toyli DM, et al. 2012. Engineering shallow spins in diamond with nitrogen delta-doping. *Appl. Phys. Lett.* 101:082413
25. Ohashi K, Rosskopf T, Watanabe H, Loretz M, Tao Y, et al. 2013. Negatively charged nitrogen-vacancy centers in a 5-nm-thin ¹²C diamond film. *Nano Lett.* 13:4733–38
26. Ofori-Okai BK, Pezzagna S, Chang K, Loretz M, Schirhagl R, et al. 2012. Spin properties of very shallow nitrogen vacancy defects in diamond. *Phys. Rev. B* 86:081406
27. Krueger A, Liang Y, Jarre G, Stegk J. 2006. Surface functionalisation of detonation diamond suitable for biological applications. *J. Mater. Chem.* 16:2322–28
28. Hauf MV, Grotz B, Naydenov B, Dankerl M, Pezzagna S, et al. 2011. Chemical control of the charge state of nitrogen-vacancy centers in diamond. *Phys. Rev. B* 83:081304
29. Krueger A, Lang D. 2012. Functionality is key: recent progress in the surface modification of nanodiamond. *Adv. Funct. Mater.* 22:890–906

30. Ushizawa K, Sato Y, Mitsumori T, Machinami T, Ueda T, Ando T. 2002. Covalent immobilization of DNA on diamond and its verification by diffuse reflectance infrared spectroscopy. *Chem. Phys. Lett.* 351:105–8
31. Krueger A, Stegk J, Liang YJ, Lu L, Jarre G. 2008. Biotinylated nanodiamond: simple and efficient functionalization of detonation diamond. *Langmuir* 24:4200–4
32. Krueger A, Boedeker T. 2008. Deagglomeration and functionalisation of detonation nanodiamond with long alkyl chains. *Diam. Relat. Mater.* 17:1367–70
33. Liu Y, Gu ZN, Margrave JL, Khabashesku VN. 2004. Functionalization of nanoscale diamond powder: fluoro-, alkyl-, amino-, and amino acid-nanodiamond derivatives. *Chem. Mater.* 16:3924–30
34. Mohan N, Chen CS, Hsieh HH, Wu YC, Chang HC. 2010. In vivo imaging and toxicity assessments of fluorescent nanodiamonds in *Caenorhabditis elegans*. *Nano Lett.* 10:3692–99
35. Liu KK, Chen F, Chen PY, Lee TJF, Cheng CL, et al. 2008. Alpha-bungarotoxin binding to target cell in a developing visual system by carboxylated nanodiamond. *Nanotechnology* 19:205102
36. **Fu CC, Lee HY, Chen K, Lim TS, Wu HY, et al. 2007. Characterization and application of single fluorescent nanodiamonds as cellular biomarkers. *Proc. Natl. Acad. Sci. USA* 104:727–32**
37. McGuinness LP, Yan Y, Stacey A, Simpson DA, Hall LT, et al. 2011. Quantum measurement and orientation tracking of fluorescent nanodiamonds. *Nat. Nanotechnol.* 6:358–63
38. Faklaris O, Garrot D, Joshi V, Druon F, Boudou JP, et al. 2008. Detection of single photoluminescent diamond nanoparticles in cells and study of the internalization pathway. *Small* 4:2236–39
39. Chao JI, Perevedentseva E, Chung PH, Liu KK, Cheng CY, et al. 2007. Nanometer-sized diamond particle as a probe for biolabeling. *Biophys. J.* 93:2199–208
40. Mkandawire M, Pohl A, Gubarevich T, Lapina V, Appelhans D, et al. 2009. Selective targeting of green fluorescent nanodiamond conjugates to mitochondria in HeLa cells. *J. Biophotonics* 2:596–606
41. Gali A, Fyta M, Kaxiras E. 2008. Ab initio supercell calculations on nitrogen-vacancy center in diamond. *Phys. Rev. B* 77:155206
42. Smeltzer B, Childress L, Gali A. 2011. ^{13}C hyperfine interactions in the nitrogen-vacancy centre in diamond. *New J. Phys.* 13:025021
43. Manson N, Harrison J, Sellars M. 2006. Nitrogen-vacancy center in diamond: model of the electronic structure. *Phys. Rev. B* 74:104303
44. Beveratos A, Brouri R, Gacoin T, Poizat JP, Grangier P. 2001. Nonclassical radiation from diamond nanocrystals. *Phys. Rev. A* 64:061802
45. Robledo L, Bernien H, van der Sar T, Hanson R. 2011. Spin dynamics in the optical cycle of single nitrogen-vacancy centres in diamond. *New J. Phys.* 13:025013
46. Jarmola A, Acosta VM, Jensen K, Chemerisov S, Budker D. 2012. Temperature- and magnetic-field-dependent longitudinal spin relaxation in nitrogen-vacancy ensembles in diamond. *Phys. Rev. Lett.* 108:197601
47. Köhler J. 1999. Magnetic resonance of a single molecular spin. *Phys. Rep.* 310:261–339
48. **Degen CL. 2008. Scanning magnetic field microscope with a diamond single-spin sensor. *Appl. Phys. Lett.* 92:243111**
49. Taylor JM, Cappellaro P, Childress L, Jiang L, Budker D, et al. 2008. High-sensitivity diamond magnetometer with nanoscale resolution. *Nat. Phys.* 4:810–16
50. Budker D, Romalis M. 2007. Optical magnetometry. *Nat. Phys.* 3:227–34
51. De Zanche N, Barmet C, Nordmeyer-Massner JA, Pruessmann KP. 2008. NMR probes for measuring magnetic fields and field dynamics in MR systems. *Magn. Reson. Med.* 60:176–86
52. **Balasubramanian G, Chan IY, Kolesov R, Al-Hmoud M, Tisler J, et al. 2008. Nanoscale imaging magnetometry with diamond spins under ambient conditions. *Nature* 455:648–51**
53. **Grinolds MS, Hong S, Maletinsky P, Luan L, Lukin MD, et al. 2013. Nanoscale magnetic imaging of a single electron spin under ambient conditions. *Nat. Phys.* 9:215–19**
54. **Mamin HJ, Kim M, Sherwood MH, Rettner CT, Ohno K, et al. 2013. Nanoscale nuclear magnetic resonance with a nitrogen-vacancy spin sensor. *Science* 339:557–60**
55. **Staudacher T, Shi F, Pezzagna S, Meijer J, Du J, et al. 2013. Nuclear magnetic resonance spectroscopy on a (5-nanometer)³ sample. *Science* 339:561–63**

36. Provides one of the first applications of nanodiamonds as fluorescent biomarkers.

48. Provides the original proposal of scanning magnetic sensing with a single NV center.

52. Along with Ref. 74, presents the first experimental demonstration of magnetic sensing with a single NV center.

53. Demonstrates scanning magnetometry of a single electron spin from a 50-nm distance.

54. Along with Ref. 55, provides an experimental demonstration of nanoscale NMR with a single NV center.

56. Demonstrates electric field sensitivity of the NV center.

59. Demonstrates temperature sensitivity of the NV center.

74. Along with Ref. 52, presents the first experimental demonstration of magnetic sensing with a single NV center.

76. Provides ion concentration measurements with Gd^{3+} , Mn^{2+} , and O_2 .

56. van Oort E, Glasbeek M. 1990. Electric-field-induced modulation of spin echoes of N-V centers in diamond. *Chem. Phys. Lett.* 168:529–32
57. Dolde F, Fedder H, Doherty MW, Noebauer T, Rempp F, et al. 2011. Electric-field sensing using single diamond spins. *Nat. Phys.* 7:459–63
58. Epstein RJ, Mendoza FM, Kato YK, Awschalom DD. 2005. Anisotropic interactions of a single spin and dark-spin spectroscopy in diamond. *Nat. Phys.* 1:94–98
59. Acosta VM, Bauch E, Ledbetter MP, Waxman A, Bouchard LS, Budker D. 2010. Temperature dependence of the nitrogen-vacancy magnetic resonance in diamond. *Phys. Rev. Lett.* 104:070801
60. Chen XD, Dong CH, Sun FW, Zou CL, Cui JM, et al. 2011. Temperature dependent energy level shifts of nitrogen-vacancy centers in diamond. *Appl. Phys. Lett.* 99:161903
61. Toyli DM, de las Casas CF, Christle DJ, Dobrovitski VV, Awschalom DD. 2013. Fluorescence thermometry enhanced by the quantum coherence of single spins in diamond. *Proc. Natl. Acad. Sci. USA* 110:8417–21
62. Kucsko G, Maurer PC, Yao NY, Kubo M, Noh HJ, et al. 2013. Nanometer scale quantum thermometry in a living cell. *Nature* 500:54–58
63. Neumann P, Jakobi I, Dolde F, Burk C, Reuter R, et al. 2013. High-precision nanoscale temperature sensing using single defects in diamond. *Nano Lett.* 13:2738–42
64. Doherty MW, Struzhkin VV, Simpson DA, McGuinness LP, Meng Y, et al. 2013. Electronic properties and metrology of the diamond NV- center under pressure. arXiv:1305.2291
65. Tamarat P, Gaebel T, Rabeau JR, Khan M, Greentree AD, et al. 2006. Stark shift control of single optical centers in diamond. *Phys. Rev. Lett.* 97:083002
66. Maes J, Iakubovskii K, Hayne M, Stesmans A, Moshchalkov VV. 2004. Diamond as a magnetic field calibration probe. *J. Phys. D* 37:1102–6
67. Maze JR, Gali A, Togan E, Chu Y, Trifonov A, et al. 2011. Properties of nitrogen-vacancy centers in diamond: the group theoretic approach. *New J. Phys.* 13:025025
68. Schoenfeld RS, Harneit W. 2011. Real time magnetic field sensing and imaging using a single spin in diamond. *Phys. Rev. Lett.* 106:030802
69. Häberle T, Schmid-Lorch D, Karrai K, Reinhard F, Wrachtrup J. 2013. High-dynamic-range imaging of nanoscale magnetic fields using optimal control of a single qubit. *Phys. Rev. Lett.* 111:170801
70. Maertz BJ, Wijnheijmer AP, Fuchs GD, Nowakowski ME, Awschalom DD. 2010. Vector magnetic field microscopy using nitrogen vacancy centers in diamond. *Appl. Phys. Lett.* 96:092504
71. Steinert S, Dolde F, Neumann P, Aird A, Naydenov B, et al. 2010. High sensitivity magnetic imaging using an array of spins in diamond. *Rev. Sci. Instrum.* 81:043705
72. Acosta VM, Bauch E, Jarmola A, Zipp LJ, Ledbetter MP, Budker D. 2010. Broadband magnetometry by infrared-absorption detection of nitrogen-vacancy ensembles in diamond. *Appl. Phys. Lett.* 97:174104
73. Slichter CP. 1990. *Principles of Magnetic Resonance*. New York: Springer. 3rd ed.
74. Maze JR, Stanwix PL, Hodges JS, Hong S, Taylor JM, et al. 2008. Nanoscale magnetic sensing with an individual electronic spin in diamond. *Nature* 455:644–47
75. De Lange G, Riste D, Dobrovitski VV, Hanson R. 2011. Single-spin magnetometry with multipulse sensing sequences. *Phys. Rev. Lett.* 106:080802
76. Steinert S, Ziem F, Hall LT, Zappe A, Schweikert M, et al. 2013. Magnetic spin imaging under ambient conditions with sub-cellular resolution. *Nat. Commun.* 4:1607
77. Loretz M, Rosskopf T, Degen CL. 2013. Radio-frequency magnetometry using a single electron spin. *Phys. Rev. Lett.* 110:017602
78. Weinmann HJ, Brasch RC, Press WR, Wesbey GE. 1984. Characteristics of gadolinium-DTPA complex: a potential NMR contrast agent. *Am. J. Roentgenol.* 142:619–24
79. McGuinness LP, Hall LT, Stacey A, Simpson DA, Hill CD, et al. 2013. Ambient nanoscale sensing with single spins using quantum decoherence. *New J. Phys.* 15:073042
80. Ermakova A, Pramanik G, Cai J, Algara-Siller G, Kaiser U, et al. 2013. Detection of a few metallo-protein molecules using color centers in nanodiamonds. *Nano Lett.* 13:3305–9
81. Toyli DM, Weis CD, Fuchs GD, Schenkel T, Awschalom DD. 2010. Chip-scale nanofabrication of single spins and spin arrays in diamond. *Nano Lett.* 10:3168–72

82. Le Sage D, Arai K, Glenn DR, Devience SJ, Pham LM, et al. 2013. Optical magnetic imaging of living cells. *Nature* 496:486–89
83. Horowitz VR, Aleman BJ, Christle DJ, Cleland AN, Awschalom DD. 2012. Electron spin resonance of nitrogen-vacancy centers in optically trapped nanodiamonds. *Proc. Natl. Acad. Sci. USA* 109:13493–97
84. Geiselmann M, Juan ML, Renger J, Say JM, Brown LJ, et al. 2013. Three-dimensional optical manipulation of a single electron spin. *Nat. Nanotechnol.* 8:175–79
85. Chang K. 2010. Private communication
86. Kaufmann S, Simpson DA, Hall LT, Perunovic V, Senn P, et al. 2013. Detection of atomic spin labels in a lipid bilayer using a single-spin nanodiamond probe. *Proc. Natl. Acad. Sci. USA* 110:10894–98
87. Plakhotnik T, Gruber D. 2010. Luminescence of nitrogen-vacancy centers in nanodiamonds at temperatures between 300 and 700 K: perspectives on nanothermometry. *Phys. Chem. Chem. Phys.* 12:9751–56
88. Chernobrod BM, Berman GP. 2005. Spin microscope based on optically detected magnetic resonance. *J. Appl. Phys.* 97:014903
89. Rondin L, Tetienne JP, Spinicelli P, DalSavio C, Karrai K, et al. 2012. Nanoscale magnetic field mapping with a single spin scanning probe magnetometer. *Appl. Phys. Lett.* 100:153118
90. Maletinsky P, Hong S, Grinolds MS, Hausmann B, Lukin MD, et al. 2012. A robust scanning diamond sensor for nanoscale imaging with single nitrogen-vacancy centres. *Nat. Nanotechnol.* 7:320–24
91. Rondin L, Tetienne JP, Rohart S, Thiaville A, Hingant T, et al. 2013. Stray-field imaging of magnetic vortices with a single diamond spin. *Nat. Commun.* 4:2279
92. Jelezko F. 2013. Private communication
93. Poggio M, Degen CL. 2010. Force-detected nuclear magnetic resonance: recent advances and future challenges. *Nanotechnology* 21:342001
94. Rosskopf T, Dussaux A, Ohashi K, Loretz M, Schirhagl R, et al. 2013. On the surface paramagnetism of diamond. arXiv:1311.2036
95. Hossain FM, Doherty MW, Wilson HF, Hollenberg LCL. 2008. Ab initio electronic and optical properties of the $N-V^-$ center in diamond. *Phys. Rev. Lett.* 101:226403
96. Maier F, Riedel M, Mantel B, Ristein J, Ley L. 2000. Origin of surface conductivity in diamond. *Phys. Rev. Lett.* 85:3472–75
97. Bradac C, Gaebel T, Naidoo N, Sellars MJ, Twamley J, et al. 2010. Observation and control of blinking nitrogen-vacancy centres in discrete nanodiamonds. *Nat. Nanotechnol.* 5:345–49
98. Cui S, Hu EL. 2013. Increased negatively charged nitrogen-vacancy centers in fluorinated diamond. *Appl. Phys. Lett.* 103:051603
99. Tetienne JP, Hingant T, Rondin L, Cavaills A, Mayer L, et al. 2013. Spin relaxometry of single nitrogen-vacancy defects in diamond nanocrystals for magnetic noise sensing. *Phys. Rev. B* 87:235436
100. Samsonenko ND, Zhmykhov GV, Zon VS, Aksenov VK. 1979. Characteristic features of the electron-paramagnetic resonance of the surface centers of diamond. *J. Struct. Chem.* 20:951–53
101. Grinolds M. 2013. Private communication
102. Toyli DM, Christle DJ, Alkauskas A, Buckley BB, van de Walle CG, Awschalom DD. 2012. Measurement and control of single nitrogen-vacancy center spins above 600 K. *Phys. Rev. X* 2:031001



Contents

A Journey Through Chemical Dynamics <i>William H. Miller</i>	1
Chemistry of Atmospheric Nucleation: On the Recent Advances on Precursor Characterization and Atmospheric Cluster Composition in Connection with Atmospheric New Particle Formation <i>M. Kulmala, T. Petäjä, M. Ehn, J. Thornton, M. Sipilä, D.R. Worsnop, and V.-M. Kerminen</i>	21
Multidimensional Time-Resolved Spectroscopy of Vibrational Coherence in Biopolyenes <i>Tiago Buckup and Marcus Motzkus</i>	39
Phase Separation in Bulk Heterojunctions of Semiconducting Polymers and Fullerenes for Photovoltaics <i>Neil D. Treat and Michael L. Chabinyc</i>	59
Nitrogen-Vacancy Centers in Diamond: Nanoscale Sensors for Physics and Biology <i>Romana Schirbagl, Kevin Chang, Michael Loretz, and Christian L. Degen</i>	83
Superresolution Localization Methods <i>Alexander R. Small and Raghuveer Parthasarathy</i>	107
The Structure and Dynamics of Molecular Excitons <i>Christopher J. Bardeen</i>	127
Advanced Potential Energy Surfaces for Condensed Phase Simulation <i>Omar Demerdash, Eng-Hui Yap, and Teresa Head-Gordon</i>	149
Ion Mobility Analysis of Molecular Dynamics <i>Thomas Wyttenbach, Nicholas A. Pierson, David E. Clemmer, and Michael T. Bowers</i>	175
State-to-State Spectroscopy and Dynamics of Ions and Neutrals by Photoionization and Photoelectron Methods <i>Cheuk-Yiu Ng</i>	197
Imaging Fluorescence Fluctuation Spectroscopy: New Tools for Quantitative Bioimaging <i>Nirmalya Bag and Thorsten Wobland</i>	225

Elucidation of Intermediates and Mechanisms in Heterogeneous Catalysis Using Infrared Spectroscopy <i>Aditya Savara and Eric Weitz</i>	249
Physicochemical Mechanism of Light-Driven DNA Repair by (6-4) Photolyases <i>Shirin Faraji and Andreas Dreuw</i>	275
Advances in the Determination of Nucleic Acid Conformational Ensembles <i>Loïc Salmon, Shan Yang, and Hashim M. Al-Hashimi</i>	293
The Role of Ligands in Determining the Exciton Relaxation Dynamics in Semiconductor Quantum Dots <i>Mark D. Peterson, Laura C. Cass, Rachel D. Harris, Kedy Edme, Kimberly Sung, and Emily A. Weiss</i>	317
Laboratory-Frame Photoelectron Angular Distributions in Anion Photodetachment: Insight into Electronic Structure and Intermolecular Interactions <i>Andrei Sanov</i>	341
Quantum Heat Engines and Refrigerators: Continuous Devices <i>Ronnie Kosloff and Amikam Levy</i>	365
Approaches to Single-Nanoparticle Catalysis <i>Justin B. Sambur and Peng Chen</i>	395
Ultrafast Carrier Dynamics in Nanostructures for Solar Fuels <i>Jason B. Baxter, Christiaan Richter, and Charles A. Schmuttenmaer</i>	423
Nucleation in Polymers and Soft Matter <i>Xiaofei Xu, Christina L. Ting, Isamu Kusaka, and Zhen-Gang Wang</i>	449
H- and J-Aggregate Behavior in Polymeric Semiconductors <i>Frank C. Spano and Carlos Silva</i>	477
Cold State-Selected Molecular Collisions and Reactions <i>Benjamin K. Stuhl, Matthew T. Hummon, and Jun Ye</i>	501
Band Excitation in Scanning Probe Microscopy: Recognition and Functional Imaging <i>S. Jesse, R.K. Vasudevan, L. Collins, E. Strelcov, M.B. Okatan, A. Belianinov, A.P. Baddorf, R. Proksch, and S.V. Kalinin</i>	519
Dynamical Outcomes of Quenching: Reflections on a Conical Intersection <i>Julia H. Lehman and Marsha I. Lester</i>	537
Bimolecular Recombination in Organic Photovoltaics <i>Girish Lakbhwani, Akshay Rao, and Richard H. Friend</i>	557

Mapping Atomic Motions with Ultrabright Electrons: The Chemists' Gedanken Experiment Enters the Lab Frame <i>R. J. Dwayne Miller</i>	583
Optical Spectroscopy Using Gas-Phase Femtosecond Laser Filamentation <i>Johanan Odbner and Robert Levis</i>	605

Indexes

Cumulative Index of Contributing Authors, Volumes 61–65	629
Cumulative Index of Article Titles, Volumes 61–65	632

Errata

An online log of corrections to *Annual Review of Physical Chemistry* articles may be found at <http://www.annualreviews.org/errata/physchem>